THE ASTROPHYSICAL JOURNAL, 323:614–628, 1987 December 15

THREE-DIMENSIONAL HYDRODYNAMICAL SIMULATIONS OF STELLAR COLLISIONS. I. EQUAL-MASS MAIN-SEQUENCE STARS

W. BENZ[1] AND J. G. HILLS
Theoretical Division, Los Alamos National Laboratory
Received 1987 February 17; accepted 1987 June 17

ABSTRACT

Fully three-dimensional calculations of collisions between identical stars show two distinctly different mass-loss mechanisms. Strong shocks in nearly head-on collisions cause high-velocity jetting perpendicular to the collision axis. The mass loss in head-on collisions increases from 0.1% to 100% as the impact velocity at infinity increases from zero to 2.3 times the escape velocity from the stellar surface. The shock strength and the mass loss by jetting decrease as the impact parameter increases. However, in low-velocity encounters the mass loss increases sharply at impact parameters corresponding to nearly grazing collisions. This second mass-loss mechanism is a two-stage one in which the two stars first become gravitationally bound into a binary because of energy dissipation in the encounter, and then the binary components coalesce violently during a subsequent periastron passage. During the final merger, the two stars form a spiral-shaped mass distribution, which redistributes the angular momentum in the coalescing object within a dynamical time. The maximum mass loss by this second mechanism is about 5% by direct ejection from the system and about twice that by the formation of an accretion disk around the coalesced object. After the grazing collision, the central object shows the equatorial cusp indicative of a Roche rotational instability, and the accretion disk extends smoothly beyond the equatorial radius. The mass loss decreases rapidly at impact parameters beyond that producing maximum mass loss. Mixing is nearly complete in grazing collisions, so that the coalesced star should have nearly uniform chemical composition when it settles to the main sequence. Some blue stragglers in globular clusters must be coalesced stars. The minimum approach of two stars required for their coalescence decreases steadily from the sum of their radii for impact velocities small compared with the escape velocity from the surface of the stars to about 10% of this value at an impact velocity equal to the escape velocity. In low-velocity systems such as a globular cluster, about twice as many main-sequence stars suffer physical coalescence as form binaries by tidal capture. In higher velocity systems such as galactic nuclei, the number of binaries formed in two-body encounters is negligible compared with the number of stars undergoing collisional coalescence.

Subject headings: hydrodynamics — numerical methods — stars: binaries — stars: mass loss — stars: stellar dynamics

I. INTRODUCTION

Stellar collisions are important in galactic nuclei and the cores of globular clusters. Up to 40% of the stars in the cores of some globular clusters have suffered physical collisions (Hills and Day 1976). These authors note that some blue stragglers in globular clusters must be produced by the collisional coalescence of stars.

Stellar collisions may be even more important in galactic nuclei. Spitzer and Saslaw (1966) suggested that energy released in stellar collisions could help to power quasars. They also noted that the gas released in collisions could settle to the center of the galactic nucleus to form new stars. Colgate (1967) suggested that collisional coalescence of stars in these systems may be frequent enough to build up stars which are sufficiently massive to become supernovae. The supernova explosions would contribute to the energetic events observed in galactic nuclei. The mass lost from colliding stars in galactic nuclei may provide the fuel to power Seyfert galaxies and other low-luminosity, old active galactic nuclei (AGNs) in which the central black hole has grown too massive to be fueled by the tidal breakup of stars and the capture of their debris (Hills 1975, 1978).

In the current paper we report the results of computer simulations of stellar collisions. These three-dimensional calculations were done at a number of different impact parameters and collision velocities.

Progress has been rather slow in this field because of its inherent difficulty and the large amount of computer time needed to simulate stellar collisions properly. All previous large-scale hydrodynamic calculations of stellar collisions were published over a decade ago. Mathis (1967) and DeYoung (1968) did one-dimensional calculations in which they estimated the effect in the other two dimensions. Mathis showed that while nuclear reactions are greatly speeded up during a collision, the resulting high temperatures and densities do not last long enough for significant production of nuclear energy. This result was used to simplify all subsequent calculations including our own.

Seidl and Cameron (1972) reduced the problem to two dimensions by considering only head-on collisions between equal-mass stars. They considered stars approximated by polytropes of index $n = 3$, while we concentrate on $n = 1.5$. We ran one case for $n = 3$. It is consistent with the results of Seidl and Cameron.

Our nonzero impact parameter calculations show a variety of phenomena not anticipated in previous analytic evaluations and in one-dimensional and two-dimensional simulations. We

[1] On leave of absence to Harvard University, 1986 September–1987 June.

find, for example, that the greatest fractional mass loss in low-velocity collisions occurs when the two stars make grazing rather than head-on encounters.

Our calculations used the smooth-particle method (Lucy 1977) with 1024 particles. Details of the method are given in the next section, which also discusses the physical assumptions and initial conditions.

In § III we present the results of our calculations.

II. COMPUTATIONAL PROCEDURE

To specify a collision completely, several quantities defining the two-star system prior to collision have to be given: relative velocity at infinity, impact parameter, the masses of the two star, and their structure. Of these parameters, we vary only the first two in this paper. At the beginning of each simulation both stars have the same mass and internal density distribution. The internal structure of each star prior to the encounter is represented by a polytropic equation of state,

$$P = A\rho^{\gamma}, \tag{2.1}$$

where $\gamma = (1 + n^{-1})$ and n is the polytropic index. We choose $n = 1.5$, which is representative of low-mass, nearly fully convective stars, such as the remaining main-sequence stars in old systems including globular clusters and galactic nuclei. It is also a good approximation to the structure of low-mass white dwarfs, so the calculations also approximate the results of collisions between two white dwarfs.

Once the stars collide, equation (2.1) is no longer valid and a more general equation of state has to be used. As a second thermodynamical variable, we choose the entropy and rewrite equation (2.1) in the form

$$P = A(S)\rho^{\gamma}, \tag{2.2}$$

where S is the specific entropy. Let us define S by the equation

$$S = (\gamma - 1)^{-1} \ln (P/\rho^{\gamma}). \tag{2.3}$$

The second law of thermodynamics gives us the rate of change of the entropy:

$$T\frac{dS}{dt} = \frac{dQ}{dt}, \tag{2.4}$$

where T is the temperature and dQ is the amount of energy absorbed by a system from its surroundings. By inserting equations (2.2) and (2.3) in equation (2.4) and using the equation of state for perfect gases, we obtain

$$\frac{dA}{dt} = \left(\frac{k}{\mu m_{\rm H}}\right)(\gamma - 1)\frac{A\rho}{P}\frac{dQ}{dt}. \tag{2.5}$$

We now have to specify the quantity dQ/dt. Rigorously, dQ/dt should contain a heating term due to dissipation in shocks, a radiative and/or convective transport term, a nuclear energy production term, and so on. However, shock heating has a time scale of the order of the collision time (which, as we shall see, is a few hours), whereas the other mechanisms have much longer time scales (Kelvin-Helmholtz time scale). While the nuclear production rate is speeded up in the collision, Mathis (1967) showed that the time over which this occurs is too short in collisions between main-sequence stars to allow significant production of nuclear energy. Therefore, we only consider in the expression for dQ/dt the heating produced by dissipation of kinetic energy in shocks for main-sequence star collisions. (Nuclear burning may be important in collisions between two white dwarfs because of their higher internal densities.) To solve the problem, the energy equation, equation (2.5), has to be solved simultaneously with the equation of motion,

$$\frac{d\boldsymbol{v}}{dt} = -\frac{1}{\rho}\nabla P - \nabla\Phi + \frac{\boldsymbol{S}_{\rm visc}}{\rho}, \tag{2.6}$$

where Φ is the gravitational potential, $\boldsymbol{S}_{\rm visc}$ is a force term due to the introduction of an artificial viscosity. In the next section we present the numerical method used to solve these equations and give the detailed expression for the various terms in equations (2.5) and (2.6).

a) *Numerical Techniques*

The numerical method used to solve these equations is the so-called smooth-particle hydrodynamics (SPH) method. This method, first proposed in the astronomical context by Lucy (1977), was shown, especially by Gingold and Monaghan in numerous papers (1979, 1981, 1982, 1983*a*, *b*), to give very good results in many different applications. Benz, Slattery, and Cameron (1986) applied this technique to the study of planetary collisions.

Since the basic principles of this method have been published previously (cf. the references listed above), we will only give a condensed description of the method. We first note that any physical quantity may be written in the form

$$A(\boldsymbol{r}) = \sum_{i=1}^{N} m_i\left[\frac{A(\boldsymbol{r}_i)}{\rho(\boldsymbol{r}_i)}\right] W(|\boldsymbol{r} - \boldsymbol{r}_i|, h),$$

where $\boldsymbol{r}_i$ are the vector positions of a set of N particles, and

$$\rho(\boldsymbol{r}_i) = \sum_{j=1}^{N} m_j W(|\boldsymbol{r}_i - \boldsymbol{r}_j|, h)$$

is the density at $\boldsymbol{r}_i$. Here $W(r, h)$ is the smoothing kernel, and h is the smoothing length. Using this formalism, we now write the equation of motion in the form

$$\frac{d\boldsymbol{v}_i}{dt} = -\sum_{j=1}^{N} m_j\left(\frac{P_j}{\rho_j^2} + \frac{P_i}{\rho_i^2}\right)\nabla_i W(r_{ij}, h) - G\sum_{j=1}^{N}\frac{M(r_{ij})}{r_{ij}^2}\hat{\boldsymbol{r}}_{ij} + (\boldsymbol{F}_i)_{\rm visc}. \tag{2.7}$$

Here

$$r_{ij} = |\boldsymbol{r}_i - \boldsymbol{r}_j|, \quad \hat{\boldsymbol{r}}_{ij} = \frac{\boldsymbol{r}_i - \boldsymbol{r}_j}{r_{ij}}.$$

The first term on the right-hand side of equation (2.7) gives the pressure gradients. The somewhat unusual form derives from the equality

$$\frac{\nabla P}{\rho} \equiv \nabla\left(\frac{P}{\rho}\right) + \frac{P}{\rho^2}(\nabla\rho)$$

proposed by Gingold and Monaghan (1982) to ensure exact conservation of linear and angular momentum. The second term is the gravitational force, for which we made use of Newton's law, since the particles are spherically symmetric. $M(r_{ij})$ is the mass of particle j within a sphere of radius r_{ij} of particle i and is given by

$$M(r_{ij}) = 4\pi\int_0^{r_{ij}} r^2\rho(r)dr = 4\pi m_j\int_0^{r_{ij}} r^2 W(r, h)dr.$$

Finally, the third term represents the force term due to artificial viscosity. As shown by Gingold and Monaghan (1983*b*), both the standard Von Neumann–Richtmyer viscous pressure and the standard bulk viscosity introduce unacceptably large post-shock oscillations. They propose a new form for the bulk viscosity:

$$(\boldsymbol{F}_i)_{\rm visc} = \sum_{j=1}^{N} \pi_{ij} m_j \nabla_i W(r_{ij}, h) .$$

Here

$$\pi_{ij} = -\frac{\alpha h c_{ij}}{\rho_{ij}} \left(\frac{\boldsymbol{v}_{ij} \cdot \boldsymbol{r}_{ij}}{r_{ij}^2 + \epsilon h^2} \right) \quad \text{if } \boldsymbol{v}_{ij} \cdot \boldsymbol{r}_{ij} < 0 ,$$

$$= 0 \quad \text{if } \boldsymbol{v}_{ij} \cdot \boldsymbol{r}_{ij} \geq 0 ,$$

and $c_{ij} = 0.5(c_i + c_j)$, where c_i is the sound speed at $\boldsymbol{r}_i$, and $\rho_{ij} = 0.5(\rho_i + \rho_j)$. In these equations ϵ and α are arbitrary numerical constants.

The symmetric form for $(\boldsymbol{F}_i)_{\rm visc}$ ensures exact conservation of linear and angular momentum. This form, which gives very good results in shock-tube problems (Gingold and Monaghan 1983*b*), is the one we adopt in our code. By specifying $(\boldsymbol{F}_i)_{\rm visc}$, it is now possible to give the form of the energy equation by noting that (Gingold and Monaghan 1983*b*)

$$\frac{dQ_i}{dt} = \frac{1}{2} \sum_{j=1}^{N} m_j \pi_{ij} \boldsymbol{v}_{ij} \cdot \nabla_i W(r_{ij}, h) .$$

Therefore, the energy equation (eq. [2.5]) becomes

$$\frac{dA_i}{dt} = \left(\frac{k}{\mu m_{\rm H}} \right) (\gamma - 1) \frac{A_i \rho_i}{P_i} \frac{1}{2} \sum_{j=1}^{N} m_j \pi_{ij} \boldsymbol{v}_{ij} \cdot \nabla_i W(r_{ij}, h) . \quad (2.8)$$

To complete the description of the problem, we need to specify the form for $W(r, h)$. Mathematically, the only constraints on $W(r, h)$ are that it should be differentiable, integrable, and normalized so that $\int W(r, h) dr = 1$, and that $\int |W(r, h)| r^2 dr < \infty$. However, only two different kernels are in common use: A Gaussian kernel (Gingold and Monaghan 1977) and an exponential kernel (Wood 1981; Benz 1984*a*; Benz, Slattery, and Cameron 1986). In this paper we use the latter, which is defined by

$$W(r, h) = \frac{e^{-r/h}}{8\pi h^3} .$$

This expression for $W(r, h)$ can be inserted in equations (2.7) and (2.8), giving these equations their final form.

Recently Gingold and Monaghan (1985) proposed that a polynomial form defined on a compact support for W would speed up computation. Recent tests confirm this conjecture. We plan to change W in subsequent computations.

Several conserved quantities may be used to check the accuracy of the integration of the equations. Mass is always conserved, since no particle is lost during simulation. The conservation of total energy is required to determine mass loss accurately. Concerning energy conservation, we noted the following trends: During the first part of a simulation (up to roughly 120 time units), which includes the actual physical collision, the variation of total energy is small (always $< 3\%$) and occurs mostly during the formation of the collisional shock. On integrating the system for hundreds of time units beyond this time, the total energy increases slowly, but almost linearly with time. As the total energy increases during this latter phase, the number of particles having sufficient energy to escape increases. This obviously indicates that we no longer have a physical solution. Fortunately, before the amount of mass loss starts to increase as a result of these numerical errors, it always reaches a value which is constant over a relatively long time. The mass loss quoted in this paper corresponds to this plateau value.

Similar behavior was observed for the total angular momentum. Very good conservation (variations $<0.8\%$) was obtained for integration up to 120 time units. The good conservation of total energy and total linear and angular momentum, as well as the various tests of the program performed elsewhere (Benz 1984*b*), gives us confidence in the results.

The SPH method may underestimate the mass loss for those encounters in which the mass loss is very low (1%). The method has difficulty modeling gas in regions in which the density is much lower than the average density in the system, so it will underestimate the mass loss if the collision is gentle enough so that the mass loss is confined to the outer layers of the star.

III. RESULTS

Our three-dimensional simulations, as well as the two-dimensional simulations of Seidl and Cameron (1972), were of equal-mass stars. We computed six principal families of encounters, with each family specified by a pre-encounter impact velocity. Within each family, we made simulations at a number of different impact parameters in order to find the cross sections for mass loss, coalescence, and other physical processes associated with stellar collisions.

Table 1 summarizes the results of the individual encounters for several values of the impact velocity at infinity in units of the escape velocity from the surface of the stars. The first column gives $R_{\rm min}$, the minimum separation of the two stars in the encounter if they were point masses. $R_{\rm min}$ was calculated analytically from the pre-encounter orbital angular momentum and kinetic energy and is given in the table in units of the sum of the radii of the two stars, $(R_1 + R_2)$. The next two columns give, respectively, the fraction of the combined mass of the two stars lost in the collision and the fraction of their mass which goes into an accretion disk around the coalesced star. The last column gives the number of stars surviving the collision. Here zero indicates total breakup of the two stars; "1" indicates their coalescence, and "2" indicates either their forming a bound binary or departing from each other in a hyperbolic orbit.

In subsequent papers we explore close encounters between unequal-mass stars, including collisions and tidal captures. We are currently making highly accurate calculations of encounters between equal-mass stars which pass too far apart for physical collisions but close enough for significant tidal dissipation. We plan to simulate collisions between main-sequence stars and giants and between white dwarfs and main-sequence stars and giants.

We can show only a small fraction of the tremendous detail found in our simulations. We describe several diverse, but representative, encounters to illustrate the physics. We give plots of mass loss and other quantitative results of these collisions as a function of $R_{\rm min}$ and impact velocity. We use these results to calculate integrated cross sections for mass loss and coalescence.

TABLE 1

COLLISIONS BETWEEN EQUAL-MASS STARS

$R_{min}/(R_1 + R_2)$	% Mass Loss		Number of Survivors
	Infinity	Disk	
$V/V_{esc} = 0.0$			
0.0	0.10	0	1
0.141	0.10	0	1
0.310	0.40	3.0	1
0.534	0.90	6.0	1
0.806	3.20	8.0	1
0.953	3.40	10.0	1
1.110	0.00	0	2
$V/V_{esc} = 0.46$			
0.0	0.5	0	1
0.068	0.5	0	1
0.369	0.9	4.0	1
0.514	2.0	7.0	1
0.665	0.0	0	2
$V/V_{esc} = 0.84$			
0.0	3.50	0	1
0.119	3.20	0	1
0.246	0.40	0.3	1
0.310	0.45	1.0	1
0.400	0.10	0	2
$V/V_{esc} = 1.12$			
0.0	10.50	0	1
0.164	5.5	0.2	1
0.307	0.80	0	2
0.489	0.60	0	2
0.596	0.20	0	2
$V/V_{esc} = 1.67$			
0.0	32.2	0	1
0.1	33	0.6	1
0.156	30.6	0	2
0.297	14.0	0	2
0.413	7.6	0	2
0.595	1.7	0	2
0.717	0.1	0	2
$V/V_{esc} = 2.33$			
0.0	100.0	0	0
0.1	100.0	0	0
0.2	98.0	0	1
0.35	61.0	0	2
0.50	52.0	0	2
0.65	42.0	0	2
0.85	0.0	0	2

a) Head-on Collisions

Our head-on three-dimensional collisions provide continuity with the two-dimensional calculations of Seidl and Cameron (1972, hereafter SC), although we approximated the pre-encounter stars as polytropes of index $n = 1.5$ and SC used $n = 3$. We used $n = 1.5$ to better model collisions between lower–main-sequence stars, which constitute most stars in globular clusters and galactic nuclei. It is also much more difficult for the smooth-particle code to simulate encounters between stars with $n = 3$ than between those with $n = 1.5$ because of the higher density contrast.

We ran one head-on collision with $n = 3$ in the limit in which the two stars hit each other at parabolic speed. Our results agree with those of SC even though our simulation began with the two stars separated by more than 10 stellar radii, while SC began with the two stars in contact. Our results should model more faithfully the tidal distortion of the stars prior to actual physical contact. We also ran our simulations for a much longer time than SC. In our calculations the stellar oscillations excited by the collision went through a number of pulsations before damping away. The models of SC were not run long enough to see any oscillations.

Shock density and temperature are highest in head-on collisions. As noted by Mathis (1967) and SC, the temperature reaches a maximum of several times 10^7 K. The nuclear reactions increase greatly during the collision, but the high rate is only maintained for a few minutes, which is too short to produce significant nuclear energy in main-sequence stars. It takes a main-sequence star a Kelvin time (about 10^7 yr for the Sun) to produce enough nuclear energy to equal its thermal energy.

Figure 1 shows the integrated system energies during a head-on collision at an impact velocity at infinity of $V = 0$ (henceforth V is used to indicate relative impact velocity at infinity), while Figure 2 shows them during a collision with $V = 1.7V_{esc}$, where

$$V_{esc} = (2M_1/R_1)^{1/2} = (2GM_2/R_2)^{1/2}$$

is the escape velocity from the surface of either star. Here M_i and R_i ($i = 1, 2$) are the masses and radii of the two stars. The time unit in these figures is approximately the pre-encounter dynamical time (oscillation time) of each star. The time unit is

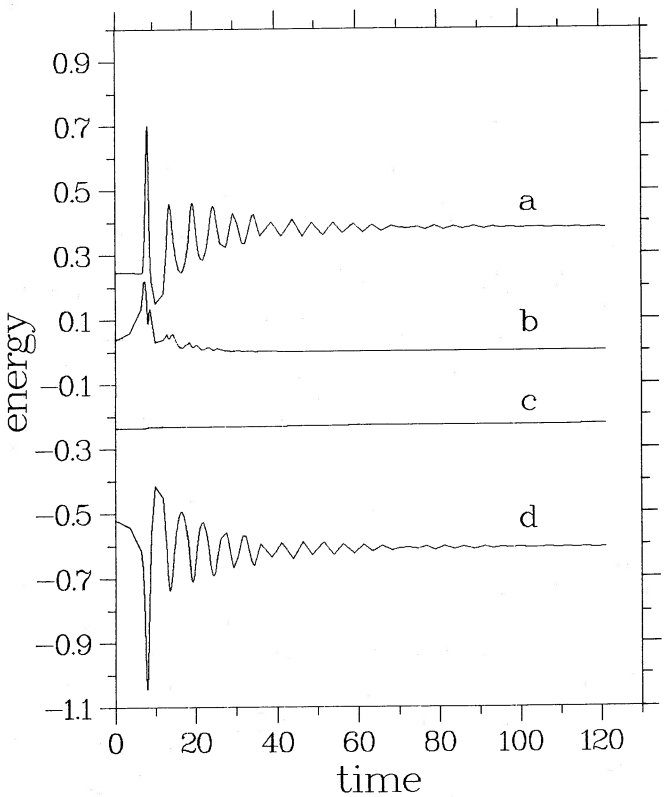

FIG. 1.—Change in the energies of a two-star system due to a head-on collision. The stars have equal mass, and the impact velocity at infinity is zero, so the two equal-mass stars hit each other at the parabolic velocity. Here curves *a*, *b*, and *d* show, respectively, the total thermal, large-scale kinetic, and gravitational potential energies of the system, while curve *c* gives the sum of these energies.

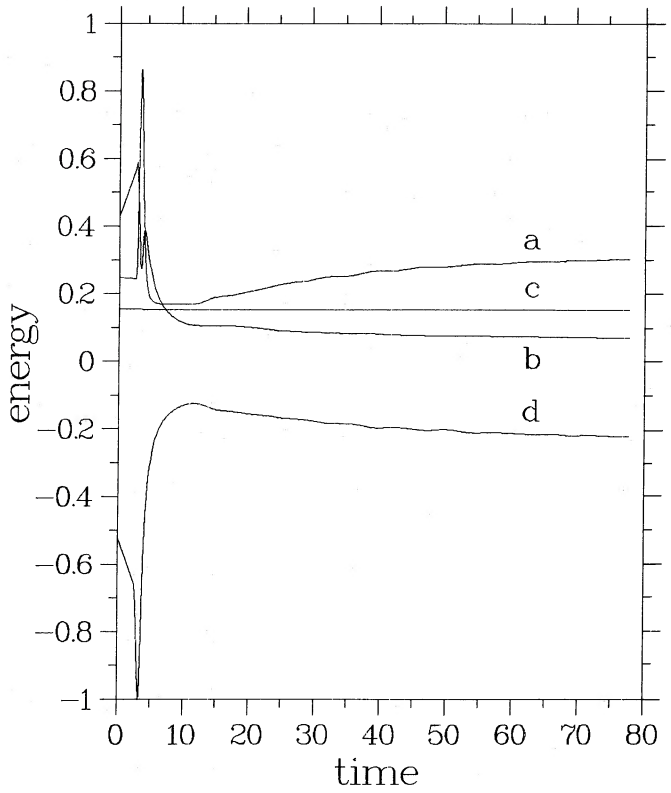

FIG. 2.—Same as Fig. 1, except that the impact velocity at infinity is 1.67 times the surface escape velocity.

related to the physical parameters of the stars by the equation

$$\tau = 1351[(M/M_\odot)(R_\odot/R)^3]^{-1/2} \text{ s} .$$

Curve c in each figure shows the total (gravitational plus kinetic plus thermal) energy. If there were no integration errors, it would be constant. Curve b shows the macroscopic kinetic energy of the two-star system. As Figure 1 shows, it rises sharply as the two stars accelerate toward each other by their gravitational attraction; then it dissipates in the physical collision. Curves a and d show, respectively, the total thermal and gravitational potential energies. The collision-induced radial oscillations of the coalesced star are clearly shown by the anticorrelated periodic variations in the thermal and potential energies.

If, for example, two identical main-sequence stars with mass $M = 0.6\ M_\odot$ and radius $R = 0.7\ R_\odot$ collide, the time unit is $\tau = 1021\ s = 17$ minutes. If they collide at parabolic speed, then Figure 1 shows the system energies during the collision. This simulation covered about 120 time units, or 34 hr in real time. From the variations in the potential energy, we see that the coalesced object stops oscillating and reaches dynamical equilibrium after about 70 time units or 20 hr. Its radius is larger than that of the two stars prior to the collision, and its density is less. Because the collision is head-on, the coalesced object acquires no angular momentum and does not rotate.

We note the very short time required for these two stars to collide, oscillate, and finally reach dynamical equilibrium. This short time confirms that neglecting heat transport is a good approximation. We expect the coalesced star to radiate away its excess energy to become a main-sequence star with a mass of $1.2\ M_\odot$ for $V/V_{esc} = 0$ or with a mass of $0.8\ M_\odot$ for $V/V_{esc} = 1.7$ after a Kelvin-Helmholtz (thermal) time.

There are evident differences between the low-speed collision shown in Figure 1 and the high-speed one shown in Figure 2. Coherent, relatively low amplitude oscillations, which any theorist could snuggle up to, are produced in the low-speed collision. The high-speed collision produces a mess. It is the epitome of a nonlinear phenomenon. The kinetic energy of this impact exceeds the binding energy of the two stars, but a single, coalesced object with about 0.7 times the integrated mass of the two stars survives the collision. The amplitudes of its radial oscillations are large, and its various layers oscillate with different periods, so there is no coherent, overall pulsation evident in its integrated energies.

More than 30% of the mass of the two stars escapes the system shown in Figure 2, and much of the rest rains back on the coalesced object over a time which is much longer than the pulsation time of the star. This raining back on the central object is responsible for the progressive increase in its thermal energy, and the corresponding decrease in its potential energy shown in Figure 2.

i) *Jetting*

As the approaching hemispheres of the two stars plunge into each other, an oblique shock forms at the interface, causing jetting in the plane perpendicular to the line of centers of the two stars. The velocity of some of the jetted material exceeds the impact velocity of the two stars. Jetting is the principal mass-loss mechanism in head-on collisions. It was already evident in the work of SC. The specific energy of the high-velocity jetted material is much larger than the average specific energy in the stars, so jetting increases the gravitational binding energy of any coalesced star that survives the collision. Jetting permits survival of the system shown in Figure 2 even though its total energy is positive. Jetting in oblique shock has been known to the defense community for decades and is used in armor-piercing projectiles. The impact of a properly shaped projectile causes a jet of metal to penetrate the armor at a speed several times that of the projectile. Jetting occurs in meteor impacts and is likely responsible for lunar rays and for the large-scale distribution of tektites on the Earth, and it may be responsible for the ejections of the meteorites from Mars which have been found recently in Antarctica.

ii) *Mass Loss*

To determine the amount of mass loss, we first find the fraction of the total mass which is energetically capable of escaping, as was done by SC. For each particle we compute the expression

$$T_i + P_i/(\gamma - 1) + \rho_i \Phi_i = E_i ,$$

where T_i is the outgoing kinetic energy defined by

$$T_i = \begin{cases} 0 & \text{if } x^i v_x^i,\ y^i v_y^i, \text{ or } z^i v_z^i < 0 , \\ \rho_i[(v_x^i)^2 + (v_y^i)^2 + (v_z^i)^2]/2 & \text{otherwise} . \end{cases}$$

Here (x^i, y^i, z^i) and (v_x^i, v_y^i, v_z^i) are the coordinate and velocity components of the fluid particles in a Cartesian frame relative to the center of mass of the coalesced object, ρ_i is the particle density, and Φ_i is the gravitational potential energy.

A fluid particle is assumed to escape if $E_i > 0$. The fractional mass loss, $M(t)$, at time t is the sum of all particles having $E_i > 0$ at that time, divided by the total number of particles, since all the particles have the same mass. $M(t)$ reaches a ter-

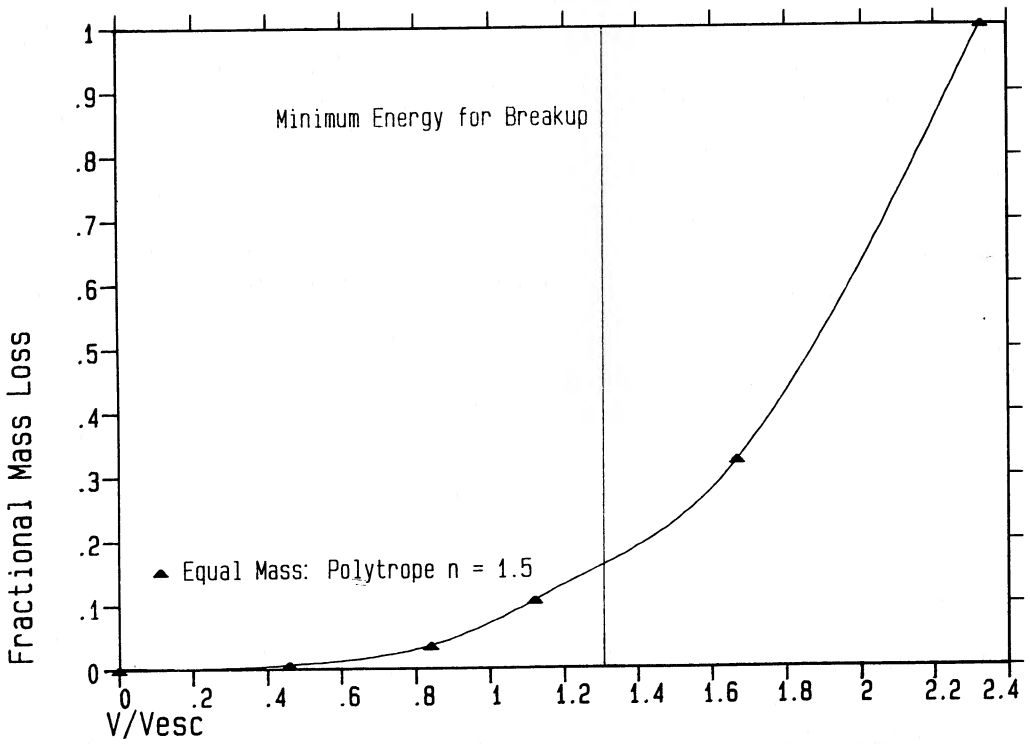

FIG. 3.—Fraction of the mass lost in a two-star, head-on collision as a function of impact velocity at infinity. The impact velocity is given in units of the escape velocity from the surface of the two stars.

minal value at large t, which we assume to be the true mass loss. (See previous discussion in § II.) This mass-loss fraction is shown in Table 1.

As shown in Figure 3, the fraction of mass lost in head-on collisions goes up with increasing impact velocity at infinity, V. The increase in V causes a corresponding increase in shock strength. Even if $V = 0$, mass loss occurs because the mutual gravitational attraction of the two stars ensures that they hit each other with at least the escape speed, V_{esc}, which exceeds the sound speed in most of the star. Some of the jetted material produced in the subsequent shock acquires a velocity high enough for escape.

The computer simulations show complete breakup of the stars in head-on collisions if V is at least $2.3V_{esc}$. The gravitational binding energy of each star is

$$E_{ib} = \frac{3}{7}\left(\frac{GM_i^2}{R_i}\right) = \frac{3}{14}(M_i V_{esc}^2) \qquad (3.1)$$

for a polytrope of index $n = 1.5$. The kinetic energy of the two stars in center-of-mass coordinates is

$$E_k = \frac{1}{2}\mu V^2 = \frac{1}{2}\left(\frac{M_1 M_2}{M_1 + M_2}\right) V^2 = \frac{1}{4} MV^2 , \qquad (3.2)$$

where $M = M_1 = M_2$. The two stars have enough kinetic energy ($E_k = 2E_{ib}$) to break up if $V = (12/7)^{1/2} V_{esc} = 1.3V_{esc}$, if none of the escaping material has positive energy (finite outflow velocity) at infinity.

At $V = 1.3V_{esc}$ the total energy of the two stars is zero, so the average energy per unit mass is just enough for escape. If half the mass has less than the mean energy and half has more, then about half the mass would escape. The computer simulations show that at $V = 1.3V_{esc}$, less than 20% of the mass escapes. This small mass loss is the result of jetting, which causes a relatively small fraction of the mass to acquire much of the kinetic energy.

b) *Effect of Impact Parameter*

Figure 4 shows the fraction of mass loss as a function of the closest approach, R_{min}, of the two stars. At high impact velocities the fraction of the mass lost decreases with increasing R_{min} as a result of a progressive weakening of the shock and of the jetting which it produces. At large impact parameters the relative motion of the two stars at closest approach is nearly parallel to their colliding surfaces, so there is no shock except in the outermost layers of the stars and little mass loss by jetting. The higher the impact velocity, the greater the value of $R_{min}/(R_1 + R_2)$ needed to weaken the shock enough to terminate mass loss by jetting. This behavior is evident in Figure 4; the rate of decrease in mass loss with increasing $R_{min}/(R_1 + R_2)$ is much less at $V/V_{esc} = 1.7$ than at $V/V_{esc} = 0.8$.

In relatively low velocity, grazing collisions the gravitational tidal pull of each star on the other is important, as is evident in the two lowest velocity families of encounters shown in Figure 4, which have $V/V_{esc} = 0$ and $V/V_{esc} = 0.46$. The impact velocities of stars in most stellar systems lie between these two values. Even in a typical galactic nucleus, $V = 200$–300 km s^{-1}, so $V/V_{esc} = 0.3$–0.5 for main-sequence stars, while in a globular cluster $V/V_{esc} = 0.02$ is typical. These two families of encounters show marked increases in mass loss as the distance of closest approach, $R_{min}/(R_1 + R_2)$, *increases* up to some critical value beyond which the mass loss drops rapidly to zero. In the limit $V = 0$, the maximum mass loss occurs if $R_{min}/(R_1 + R_2) \approx 1$, so direct physical contact is not primarily responsible for the mass loss, although the mutual tidal distortion does cause some overlap of the stellar surfaces. As we shall

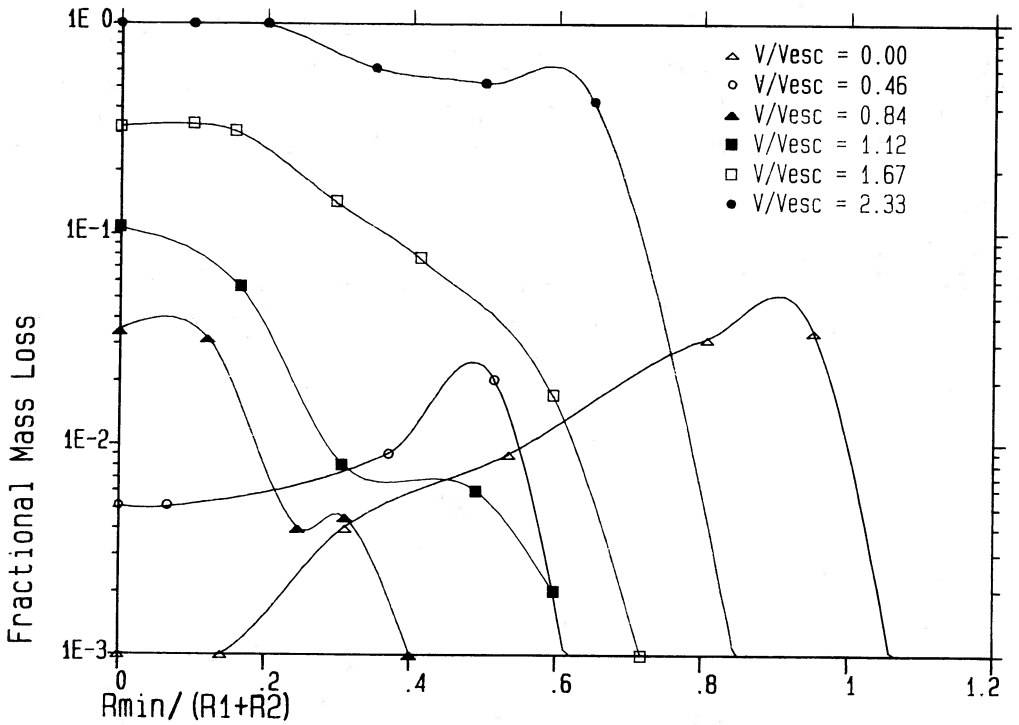

FIG. 4.—Fraction of the system mass lost as a function of R_{min}, the closest approach of the two stars in the pre-encounter orbit. Here $(R_1 + R_2)$ is the sum of the radii of the two stars. The curves are labeled according to the impact velocity at infinity in units of the escape velocity from the surface of the two stars.

show, the increased mass loss in grazing collisions is the result of a two-stage process in which a gravitationally bound binary forms by tidal dissipation during the first approach, and then the binary coalesces rather violently into a single, fast-rotating star during a subsequent periastron passage.

i) *Minimum Approach for Coalescence*

From the data in Table 1, we can estimate the minimum approach, $R_{min}/(R_1 + R_2)$, needed for coalescence. Figure 5 shows for each family of fixed impact velocities V/V_{esc} the maximum $R_{min}/(R_1 + R_2)$ for which we found coalescence and the minimum $R_{min}/(R_1 + R_2)$ for which two stars survive. We assume that the boundary between coalescence and two-star survival is halfway between these two values, as plotted in the figure. We note that the minimum $R_{min}/(R_1 + R_2)$ needed for coalescence decreases from unity for $V/V_{esc} = 0$ to 0.1 for $V/V_{esc} = 1.7$. For $V/V_{esc} = 2.3$, a close encounter with $R_{min}/(R_1 + R_2) \lesssim 0.1$ produces total breakup rather than coalescence.

ii) *Failed Binaries, Accretion Disks, and Roche Cusps*

Figure 6 shows the system energies during a grazing encounter between two stars with closest approach $R_{min}/(R_1 + R_2) = 0.953$ and impact velocity $V = 0$. The labeling of the energy curves is the same as in Figures 1 and 2. This collision produced the maximum mass loss of any member of family $V = 0$. The tidal dissipation and the shock dissipation produced by the impact of the two tidal bulges during the first periastron passage were sufficient for the two stars to become gravitationally bound in an orbit with a semimajor axis a few times larger than their radii. Curve *b*, which gives the macroscopic kinetic energy of the system, clearly shows the two periastron passages. The first peak in this curve results from the increased kinetic energy produced by the gravitational attraction of the two stars in the initial parabolic orbit. The curve is almost symmetric around the first peak because the energy dissipation is an order of magnitude less than the kinetic energy. However, the second peak is lower than the first because of the tidal dissipation during first passage. Even more rapid energy dissipation occurred during second passage.

No mass was lost during first passage. The tidal dissipation caused the radii, R_1 and R_2, of the two stars to increase as some of their internal binding energy was used to bind the two stars gravitationally into a binary. This is evident in curves *a* and *d*, which show, respectively, the thermal energy and gravitational potential energy of the two stars. The thermal energy curve shows a drop and the potential energy curve shows an increase (becomes less negative) after first periastron passage.

On the next periastron passage, which was the first one after the two stars formed a gravitationally bound binary, the encounter was much more violent. In this encounter $(R_1 + R_2)/R_{min}$ was larger because of the increase in the stellar radii, and the relative velocity of the two stars was reduced, which allowed more time for mutual gravitational perturbations.

The first five frames of Figure 7 are "snapshots" of the two stars at increasing times during second periastron passage, while the last frame shows the system long after the collision. They are projections of the fluid particle velocities onto the plane containing the center of mass of the two stars. A spiral pattern formed during second periastron passage. A spiral is very effective in redistributing angular momentum (Hills 1976), so some material was slung from the system at high specific angular momentum and kinetic energy, while the remainder coalesced into a star on the verge of rotational instability with an accretion disk orbiting it.

The two-stage process in which a binary first forms in a

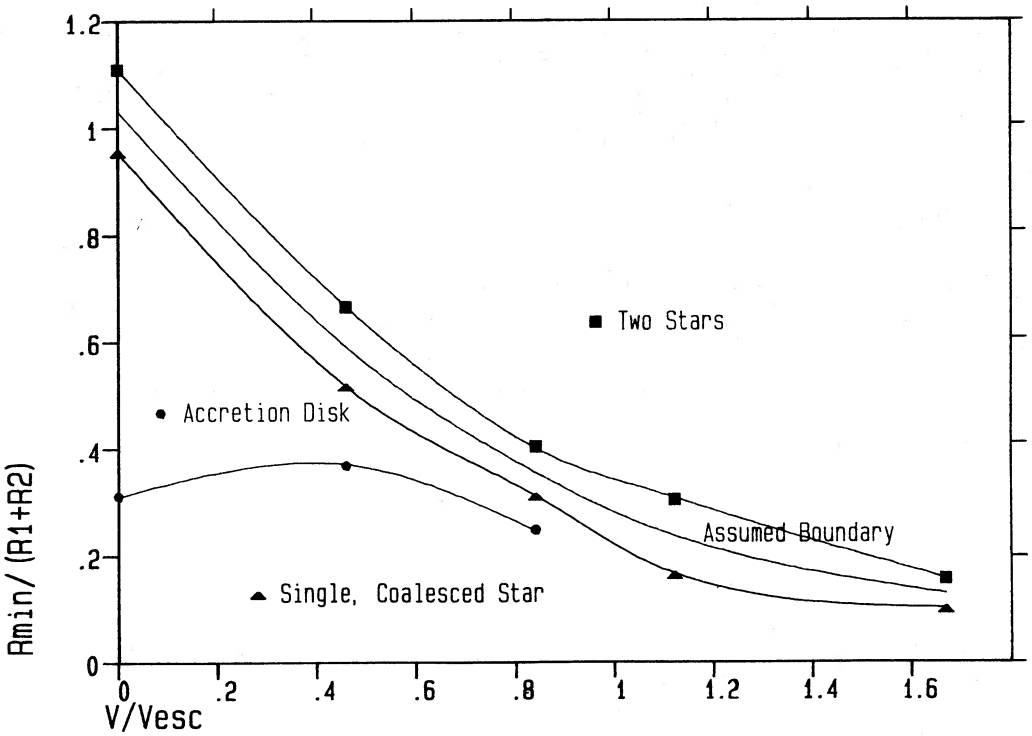

FIG. 5.—The upper diagonal curve shows the minimum value of $R_{min}/(R_1 + R_2)$ for which two stars are observed to survive the collision, while the lower diagonal curve shows the maximum value of $R_{min}/(R_1 + R_2)$ for which coalescence is observed. The middle diagonal curve is the assumed boundary between coalescence and two-star survival. The curve in the lower left-hand part of the figure gives the smallest value of R_{min} for which an accretion disk is observed around the postencounter object.

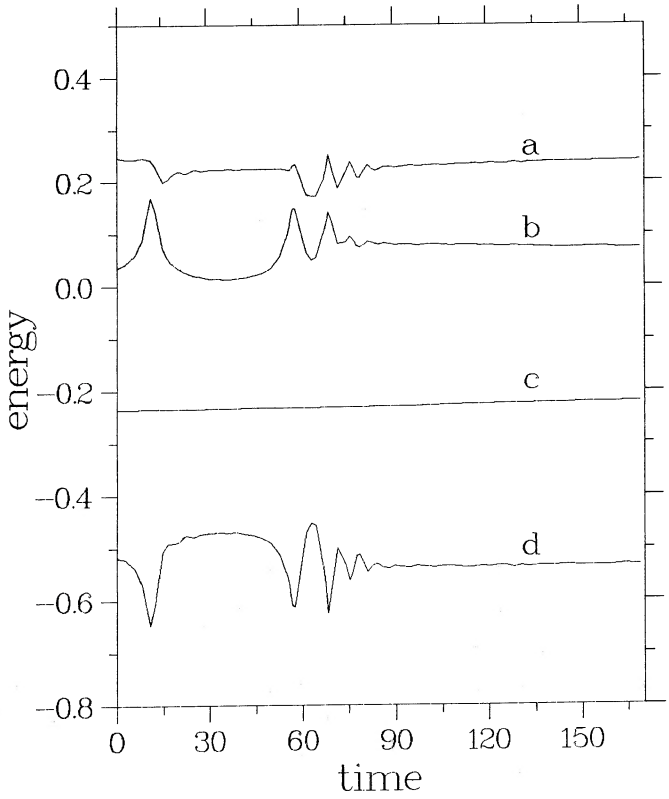

FIG. 6.—Change in system energies in a collision between two identical stars in which the impact velocity V is zero and the closest approach of the two stars is $R_{min}/(R_1 + R_2) = 0.953$. The curves are labeled as in Fig. 1. The stars become gravitationally bound during the first periastron passage and coalesce into a single star during the second periastron passage.

grazing collision, and then coalesces into a single star during a subsequent periastron passage, also occurred in families $V/V_{esc} = 0.46$, 0.84, 1.12, and 1.67 for $R_{min}/(R_1 + R_2) = 0.514$, 0.310, 0.164, and 0.1, respectively. The stars in the encounter in family $V/V_{esc} = 0.46$ only coalesced into a single star on the third periastron passage. We note that binary capture and coalescence occurred for $V/V_{esc} = 1.67$ even though the two stars have positive energy. Jetting during the first periastron passage ejected material of very high specific energy, which allowed the formation of a bound binary and final coalescence.

iii) *High-Speed, Off-Center Collisions*

Figure 8 shows the system energies in a high-speed collision ($V = 1.67V_{esc}$) in which the closest approach $R_{min}/(R_1 + R_2) = 0.413$ is too large to allow coalescence. The labeling of the energy curves is the same as in Figure 2. The two stars do not become gravitationally bound to each other, but they are significantly altered by the encounter.

About 8% of their mass is left behind as an expanding unbound cloud at the center of mass of the system. This debris cloud is somewhat elongated along the line joining the two stars.

The stars lose a significant amount of binding energy, which by the virial theorem causes both a considerable increase in their potential energy (which becomes less negative) as shown in curve *d*, and a decrease in their thermal energy as shown in curve *a*. They are larger, lower in density, and cooler than before the encounter. They also pulsate radially, as is evident by the periodic variations in their potential energy. Because of the symmetry of the encounter for equal-mass stars, the two stars pulsate in phase, although they are rapidly receding from each other.

Similar coherent, postencounter oscillations were observed

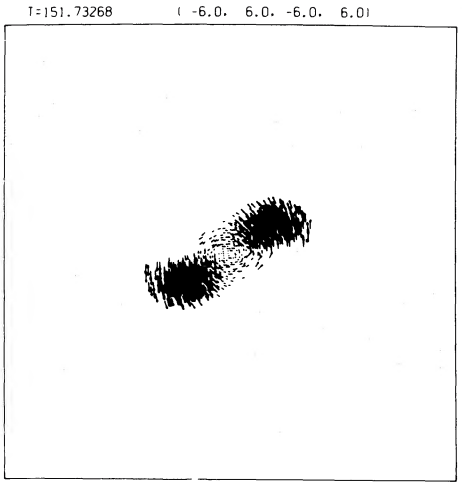

1

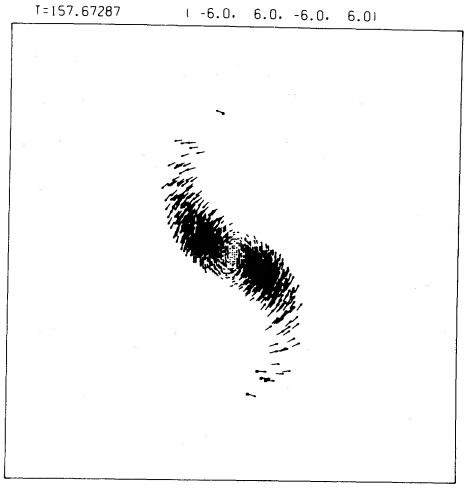

2

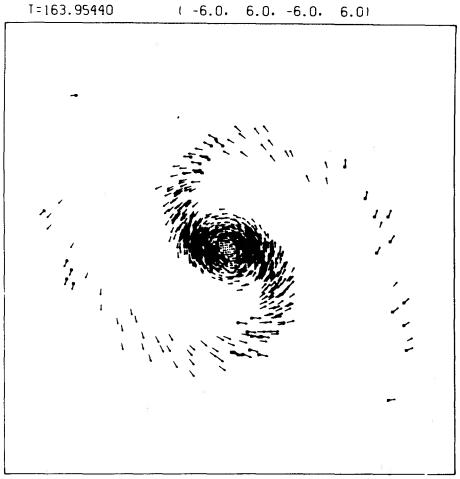

3

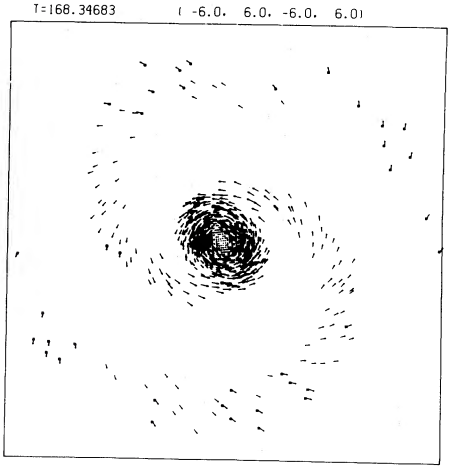

4

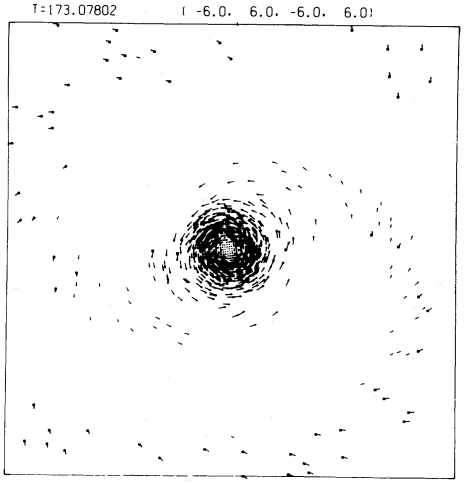

5

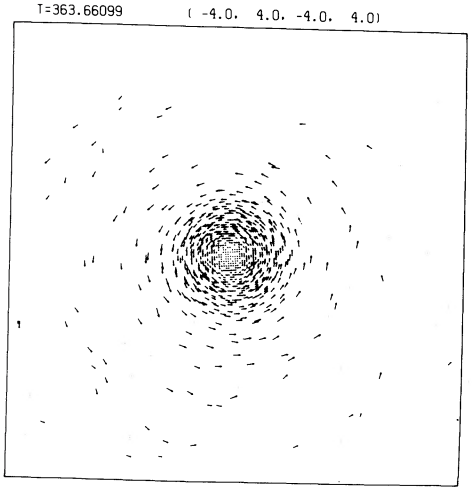

6

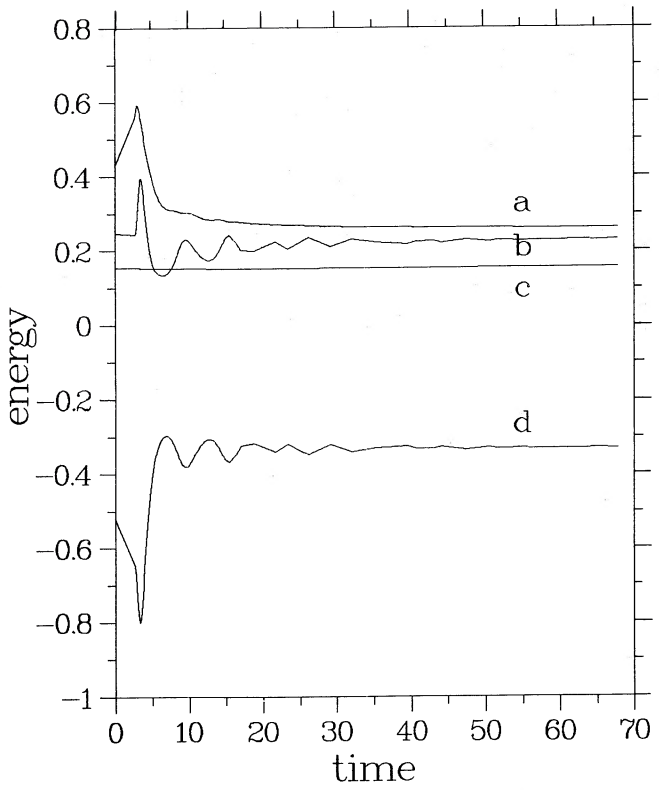

FIG. 8.—Change in system energies during a collision between two identical stars in which the impact velocity V/V_{esc} is 1.67 and the closest approach in the collision orbit is $R_{min}/(R_1 + R_2) = 0.413$. The energy curves are labeled as in Fig. 1.

for the case where $V = 1.67V_{esc}$ and $R_{min}/(R_1 + R_2) = 0.297$. Binary formation and eventual coalescence occurred in this family for $R_{min}/(R_1 + R_2) = 0.1$.

For the family $V/V_{esc} = 2.33$, total disruption occurred for $R_{min}/(R_1 + R_2) = 0.0$ and 0.1. For $R_{min}/(R_1 + R_2) = 0.2$ in this family, about 2% of the mass remained behind in a gravitationally bound cloud with a radius about a factor of 25 larger than that of the pre-encounter stars. The remainder of the mass was lost.

iv) *Accretion Disks and the Rotation of the Coalesced Star*

Figure 5 shows the wedge-shaped area of the parameter plane defined by the impact velocity V/V_{esc} and the closest approach in the pre-encounter orbit $R_{min}/(R_1 + R_2)$, in which we found the coalesced object to be on the verge of rotational instability with an accretion disk around it. The upper boundary of this area is the one defining whether one or two stars survive the encounter. The accretion disk forms only if the two stars coalesce into one. The smallest values of $R_{min}/(R_1 + R_2)$ for which we observed an accretion disk around a rotationally unstable coalesced star are about 0.3, but because of incompleteness of data they may be present at $R_{min}/(R_1 + R_2)$ as small as 0.2. The wedge extends from $V/V_{esc} = 0$ to about $V/V_{esc} = 1$. For $R_{min}/(R_1 + R_2) < 0.2$–0.3, the coalesced object does not have enough angular momentum to be rotationally unstable, so no accretion disk forms around it. For $V/V_{esc} > 1$, coalescence occurs only at such small values of $R_{min}/(R_1 + R_2)$ that the coalesced object is never rotationally unstable.

Table 1 shows the mass of the accretion disk in units of the combined mass of the two stars prior to encounter. The mass of the accretion disk tends to increase as $R_{min}/(R_1 + R_2)$ increases within the wedge-shaped area. It is especially evident for collision families $V/V_{esc} = 0$ and $V/V_{esc} = 0.46$, which have the postencounter coalesced object on the verge of rotational instability with a massive accretion disk around it for a wide range of impact parameters. The rate of rotation of the coalesced star increases with impact parameter until at about $R_{min}/(R_1 + R_2) = 0.2$–0.3 it first becomes rotationally unstable and an accretion disk forms around it. The fraction of the mass in the accretion disk increases to about 6%–7% in both these families for $R_{min}/(R_1 + R_2) = 0.5$ and reaches 10% in family $V/V_{esc} = 0$ for $R_{min}/(R_1 + R_2) = 1$. If $R_{min}/(R_1 + R_2)$ is large enough that two stars rather than one survive the encounter, these stars rotate well below the limit for rotational instability and they have no accretion disks.

In the collision family $V/V_{esc} = 0.84$ the coalesced stars have the cusp structure indicative of their being rotationally unstable as well as feeble accretion disks for $R_{min}/(R_1 + R_2) = 0.246$ and 0.310. A feeble accretion disk composed of 0.6% of the original mass formed in the family $V/V_{esc} = 1.67$ for $R_{min}/(R_1 + R_2) = 0.1$. However, the star does *not* have the cusp structure indicative of rotational instability, and the accretion disk is not coplanar with the equatorial axis. It was part of the material which rained back onto the star after a very violent collision which led to a third of the mass being ejected from the two-star system.

Figure 9 shows postencounter, fluid particle velocity projections of the coalesced object for three different impact parameters in collision family $V = 0$. Each of these three postcollision objects is on the verge of rotational instability and has an accretion disk around it. The accretion blends smoothly into the equator of the rotating star, so it is difficult to estimate the mass of the disk.

The stars of Figure 9 shows the equatorial cusp indicative of a Roche-type (cf. Ogorodnikov 1965) rotational instability which is characterizied by the outermost layer of the star having a centrifugal force at the equator which just balances gravity. This is also the situation throughout the accretion disk. This is not a global instability in the sense of the rotational bar instability (Ostriker and Peebles 1973) which occurs if the rotational energy exceeds 0.14 times the absolute value of the total potential energy. The bar instability certainly occurred during a number of collisions, as illustrated by the spiral in Figure 7. However, the final, coalesced central objects always have $\beta < 0.14$.

The coalesced star contracts to the main sequence in a Kelvin time. The contraction reduces its moment of inertia, so if it is rotationally unstable after the collision, it must shed more material at its equator into the accretion (excretion) disk as it contracts unless it can rid itself of its excess angular momentum in less than the Kelvin time. Even if the star can lose significant angular momentum, additional mass loss will be required to remove it. The mass loss shown in Table 1 assumes that all the mass in the accretion disk is retained by the star. It can only be a lower limit to the final mass loss,

FIG. 7.—Episodes in the evolution of the system shown in Fig. 6. The frames show the velocity vectors of the fluid particles projected onto the plane containing the centers of mass of the two stars. The first five frames occurred during second periastron passage, and the last was taken near the end of the computer simulation.

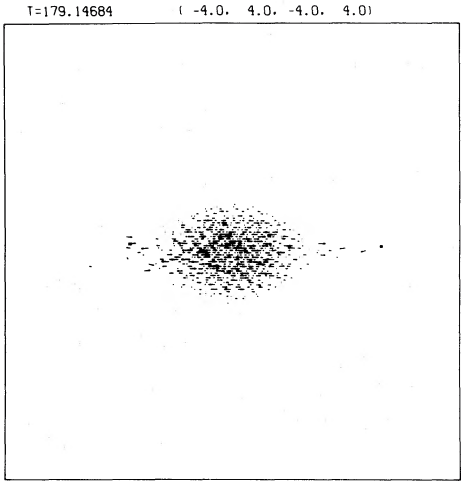

1

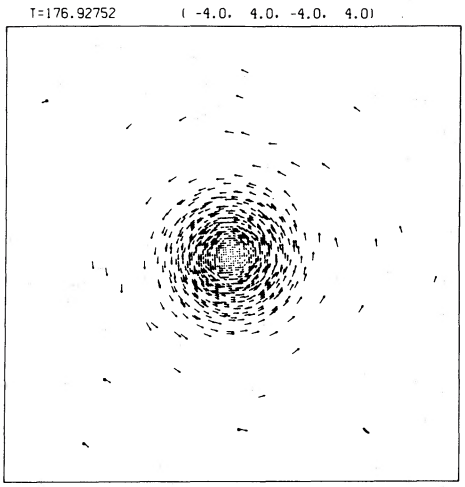

1

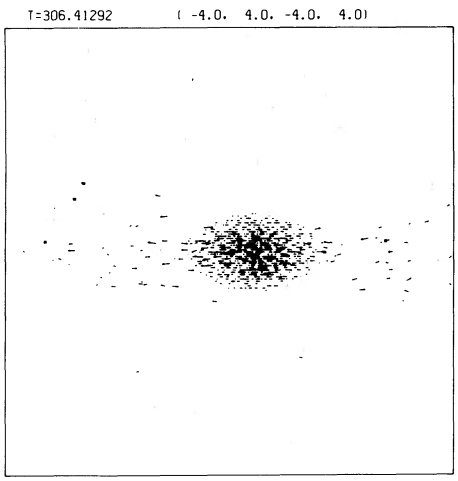

2

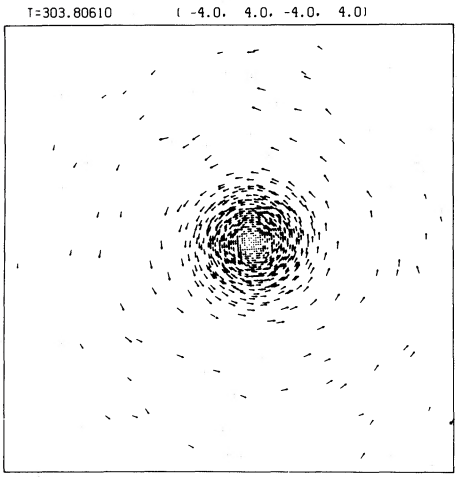

2

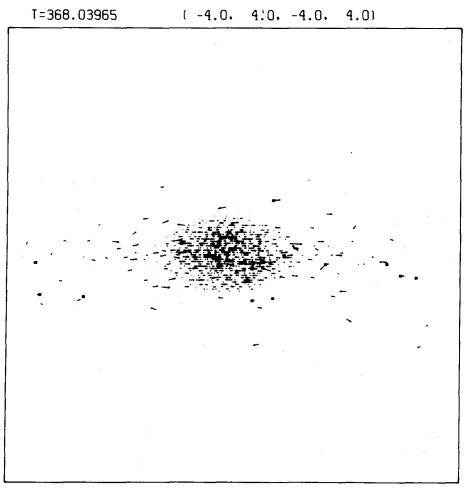

3

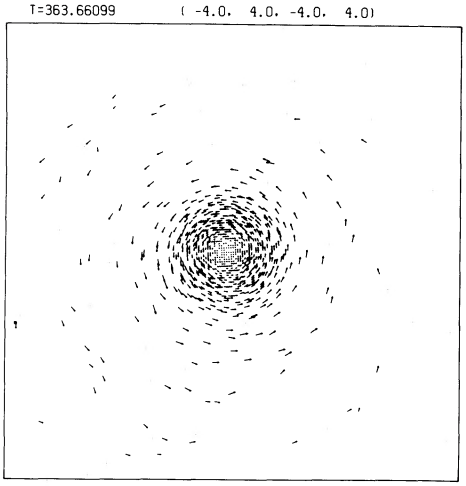

3

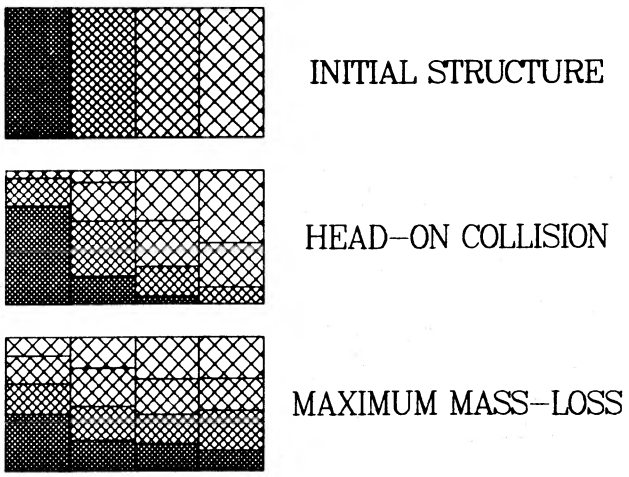

FIG. 10.—Histograms showing the degree of mixing in the coalesced stars. The first histogram shows the mass distribution in the pre-encounter stars. The second histogram shows the mass distribution in the coalesced star after a head-on collision, and the third histogram shows it after a grazing collision.

reached after the viscous time associated with the accretion disk, the Kelvin time associated with the contraction of the star to the main sequence, and perhaps a much longer stellar-wind time associated with enhanced stellar activity, which is common in fast-rotating stars.

v) *Mixing in the Coalesced Star*

The histograms in Figure 10 show the degree of physical mixing in both the head-on collision shown in Figure 1 and the grazing collision shown in Figure 2. The first histogram shows the total mass of the two pre-encounter stars divided into four equal bins in rank order of distance from the center of each star. The other two histograms show how this mass is distributed in the final coalesced star. While 80% of the mass in the inner bin of the coalesced star is from the inner bin of the pre-encounter stars in the head-on collision, less than 50% of it is from the inner bin in the grazing collision, which indicates more thorough mixing.

This work strongly suggests that stars are well mixed by grazing collisions, so nuclear waste from their cores is diluted with hydrogen-rich material from their outer layers. This mixing resets the nuclear clock of the coalesced star. The star returns to the zero-age main sequence, but with a larger helium abundance and consequently a higher luminosity than other main-sequence stars of the same mass in the stellar system. The coalesced object appears as a blue straggler if the two stars undergoing coalescence are near the top of the main sequence. This supports conjectures on blue stragglers made in Hills and Day (1976).

vi) *Tidally Captured Binaries*

If $V = 0$, the two stars must either coalesce or form a binary as any tidal dissipation causes them to become gravitationally bound. Press and Tueukolsky (1977) used analytic approximations to estimate capture cross sections as a function of V in the limit of weak tidal energy dissipation. Our present numerical simulations cannot be used to measure the small tidal energy dissipation at the large periastron distances which are needed to check their approximations. We are preparing improved computer simulations using a much larger number of fluid particles to better model distant tidal encounters.

The calculations of Press and Teukolsky (1977) were for equal-mass stars treated as polytropes of index $n = 3$. This choice is unfortunate, since main-sequence stars in globular clusters, where most tidal captures occur, are closer to polytropes of index $n = 1.5$. However, tidal dissipation is much more sensitive to the closest approach of the two stars than to internal structure, so the capture cross sections for $n = 1.5$ may not differ significantly from those calculated for $n = 3$. They find that the minimum approach required for tidal capture of two main-sequence stars decreases from $R_{\rm min}/(R_1 + R_2) = 1.5$ at $V = 10$ km s^{-1}, which is typical of the impact velocity in a globular cluster, to $R_{\rm min}/(R_1 + R_2) = 1$ at $V = 60$ km s^{-1}. The escape velocity of a main-sequence star is about $V_{\rm esc} = 600$ km s^{-1}, so tidal capture is not possible for $V/V_{\rm esc} > 0.1$ because, as shown in this paper, an encounter that is close enough to produce a binary capture leads to coalescence of the stars.

At the low impact velocities found in globular clusters, gravitational focusing is important, and the cross section for any collision process is directly proportional to the maximum value of $R_{\rm min}$ for which it occurs. (Such cross sections are discussed in § IIIc of this paper.) Since binary tidal capture in globular clusters requires $R_{\rm min}/(R_1 + R_2) \lesssim 1.5$, while coalescence occurs if $R_{\rm min}/(R_1 + R_2) \lesssim 1$, only for $R_{\rm min}/(R_1 + R_2)$ between 1.0 and 1.5 will the encounter produce a binary. It is evident that *among main-sequence stars in globular clusters, collisional coalescence is twice as frequent as tidal capture.*

The tidal energy dissipation occurring at a fixed value of $R_{\rm min}/(R_1 + R_2)$ is reduced by half if the encounter is between a white dwarf and a main-sequence star rather than between two main-sequence stars. However, the largest value of $R_{\rm min}/(R_1 + R_2)$ which still permits tidal capture decreases only about 10% in this case because of the strong dependence of the tidal energy dissipation on $R_{\rm min}/(R_1 + R_2)$. We have yet to simulate encounters between a white dwarf and a main-sequence star, but it is likely that they will coalesce only if $R_{\rm min}$ is of the order of the radius of the main-sequence star. If this is the case, in globular clusters the cross section for tidal capture of a white dwarf by a main-sequence star is about twice the cross section for coalescence.

vii) *Binary Formation and Coalescence in High-Velocity Collisions*

If $R_{\rm min}/(R_1 + R_2)$ slightly exceeds the minimum needed for coalescence, a binary may form by the energy dissipated in the physical collision of the two stars (rather than by their tidal dissipation, which was the subject of the Press-Teukolsky study). However, tidal dissipation in subsequent periastron passages may increase the radii of the stars enough for them to coalesce. This two-stage process was observed for $V/V_{\rm esc} = 0$, 0.46, 0.84, 1.12, and 1.67 at $R_{\rm min}/(R_1 + R_2) = 0.953$, 0.514, 0.310, 0.164, and 0.1, respectively. We found that if both stars survived a high-velocity encounter at a $R_{\rm min}$ larger than these values, they appeared to be in a hyperbolic orbit with respect to each other. If we explored the zone between the largest value of $R_{\rm min}/(R_1 + R_2)$ where coalescence was observed after the formation of a binary and the smallest value of $R_{\rm min}/(R_1 + R_2)$

FIG. 9.—Mass distribution in three postencounter objects in collision family $V = 0$. Objects 1, 2, and 3 were the final result of the encounters in which $R_{\rm min}/(R_1 + R_2) = 0.310$, 0.806, and 0.953, respectively. The first frame of each object is a projection of the velocities of the fluid particles onto a plane containing the rotational axis, while the other frame is a projection onto the equatorial plane. Each of the three objects is on the edge of rotational instability, and each has an accretion disk around it.

where two stars survive the encounter, we may find a range in which contact binaries form, but the available parameter space is small. We think it unlikely that binaries form by physical collisions in high-velocity ($V/V_{esc} \gtrsim 1$) systems.

We can formulate this problem more quantitatively. If no mass or angular momentum is lost from the system and we can ignore the rotation of the two stars, then the semimajor axis of the binary after circularization is given by the equation

$$a_f/R_{min} = 2 + (V/V_{esc})^2[R_{min}/(R_1 + R_2)] . \quad (3.3)$$

We see from Figure 5 that the minimum approach needed for coalescence drops from $R_{min}/(R_1 + R_2) = 0.5$ at $V/V_{esc} = 0.6$ to $R_{min}/(R_1 + R_2) = 0.1$ at $V/V_{esc} = 1.7$. We expect any binaries formed by collisions to have values of $R_{min}/(R_1 + R_2)$ only slightly larger than these values. Putting these values into the above equation gives $a_f = 2.2R_{min} = 1.1(R_1 + R_2)$ for $V/V_{esc} = 0.6$, and $a_f = 2.9R_{min} = 0.3(R_1 + R_2)$ for $V/V_{esc} = 1.7$. The final semimajor axis of the binary is of the order of or less than the sum of the radii of the two stars. Any loss of orbital angular momentum due to mass ejection or the rotation of the stars will cause the orbit to shrink further. Binary formation is probably not possible at these high impact velocities; if enough collisional energy dissipation occurs to allow binary formation, the two stars are close enough together in the final orbit to coalesce.

viii) *Stellar Radii in Tidally Captured Binaries*

If no mass or energy is lost before the orbit of a tidally captured binary is circularized, the energy difference between the initial hyperbolic orbit and the final binary orbit is at the expense of the internal gravitational binding energies of the stars. In this case, the ratio of the final to the initial radius of each star is related to the semimajor axis, a_f, of the binary orbit and the velocity of the two stars at infinity by the equation

$$R_f/R_0 = \{1 - (7/12)[R_0/a_f - (V/V_{esc})^2]\}^{-1} . \quad (3.4)$$

Tidal capture requires that $(V/V_{esc})^2 \ll 1$, so this factor may be ignored in the equation. If no angular momentum or mass is lost, we found earlier that the final semimajor axis a_f is equal to $2R_{min}$ if $(V/V_{esc})^2 \ll 1$. Because $R_{min} > 2R_0$ to avoid coalescence, it follows that $R_0/a_f \lesssim 0.25$ for all tidally captured binaries having identical companions, assuming conservation of angular momentum, energy (nothing radiated away), and mass. By the above equation, this requires that $R_f/R_0 \lesssim 1.17$, so that $2R_f = 0.6a_f$. Tidally captured binaries are clearly detached systems.

ix) *Radii of Coalesced Stars*

If only a single, coalesced star is the survivor of a collision between two stars having impact velocity greater than zero, the coalesced star is larger than a main-sequence star of the same mass. The mass distribution in the star after the encounter should be close to a polytrope of index 1.5 because the thorough mixing of the interior of the star produced by the collision requires its mass to be adiabatically distributed as is the case for a polytrope of index $n = 1.5$. Major deviations from the adiabatic equation of state would only appear after a Kelvin (radiative) time.

The radius of the coalesced star is related to the sum of the radii of the two stars that produced it by the equation

$$R_f/(R_1 + R_2) = [1 - (7/12)(V/V_{esc})^2]^{-1} . \quad (3.5)$$

This equation assumes conservation of mass and energy. If $V/V_{esc} = 0$, the final radius of the coalesced object is just the sum of the radii of the two stars. In such a collision the gain in the kinetic energy of the stars as they fall together is just compensated by the decrease in the potential energy, which becomes more negative, so the energy per unit mass in the coalesced object is the same as in the two stars prior to collision, which requires by the virial theorem that the mass-to-radius ratio in the final object be the same as in the colliding stars. If $V/V_{esc} > 0$, the binding energy per unit mass will be less than in the pre-encounter stars, and its average interior temperature is less than that of these stars. Its rate of production of nuclear energy will be smaller than the radiation loss from its surface, and it will shrink down to the main sequence in its Kelvin time.

c) Cross Sections for Mass Loss and Coalescence

From the conservation of energy and angular momentum, one can show (cf. Ogorodnikov 1965) that the closest-approach distance, R_{min}, of the two stars in their pre-encounter hyperbolic orbit is related to the impact parameter p by the equation

$$\frac{p^2}{R_{min}^2} = 1 + \left[\frac{2G(M_1 + M_2)}{V^2 R_{min}}\right], \quad (3.6)$$

or

$$p^2 = R_{min}^2 + R_{min} R_a , \quad (3.7)$$

where

$$R_a \equiv \frac{2G(M_1 + M_2)}{V^2} \quad (3.8)$$

is the "accretion" radius which allows for the increase in the collision cross section due to gravitational focusing of the two colliding objects. This equation treats the two objects as point masses in the pre-encounter orbit.

The cross section associated with the centers of mass of the two colliding objects passing within a distance R_{min} of each other is given by

$$\sigma = \pi p^2 = \pi(R_{min}^2 + R_{min} R_a) . \quad (3.9)$$

Here

$$p^2 = R_{min}^2 + R_{min}(R_1 + R_2)(V_{esc}/V)^2 , \quad (3.10)$$

where

$$V_{esc} = \left[\frac{2G(M_1 + M_2)}{R_1 + R_2}\right]^{1/2} \quad (3.11)$$

is the parabolic escape velocity of the two objects if separated by the sum of their radii, $R_1 + R_2$. For $M_1 = M_2$, V_{esc} is the surface escape velocity, which is about 600 km s^{-1} for main-sequence stars. The cross section increases enormously if the pre-encounter relative velocity V is very much less than V_{esc}.

In problems of this kind it is convenient to work in dimensionless units. In this particular case, it is useful to express the collision cross section associated with the two objects passing within distance R_{min} of each other in units of the cross section for producing a grazing collision or stronger of the two objects in the absence of gravity (billiard ball or geometric cross

section). This is given by the relation

$$\frac{\sigma}{\sigma_0} = \frac{\pi p^2}{\pi p_0^2} = \frac{\pi p^2}{\pi (R_1 + R_2)^2} = \left(\frac{R_{\min}}{R_1 + R_2}\right)^2 + \left(\frac{R_{\min}}{R_1 + R_2}\right)\left(\frac{V_{\rm esc}}{V}\right)^2 . \quad (3.12)$$

i) *Coalescence Cross Section and the Rate of Coalescence*

Calculating the cross section for physical coalescence is particularly easy. Here $R_{\rm fusion}$, the value of $R_{\min}$ to use in the above equation, is the two-star/one-star boundary value given by Figure 5. Table 2 shows $R_{\rm fusion}$ and the coalescence cross section calculated for various values of $V/V_{\rm esc}$. These cross sections are plotted in Figure 11. The cross sections approach $\pi R_{\rm fusion}^2$ if $V \gg V_{\rm esc}$. If $V \ll V_{\rm esc}$, the ratio of the cross section for passing within distance $R_{\min}$ at closest approach to the geometric (billiard-ball) cross section reduces to

$$\frac{\sigma}{\sigma_0} = \left(\frac{R_{\min}}{R_1 + R_2}\right)\left(\frac{V_{\rm esc}}{V}\right)^2 . \quad (3.13)$$

In this limit the coalescence cross section is linearly proportional to $R_{\min}$ rather than to $R_{\min}^2$. Using $R_{\min} = 1.03(R_1 + R_2)$, which is $R_{\rm fusion}$ for $V/V_{\rm esc} = 0$, gives us the coalescence cross section in the low-velocity limit,

$$\frac{\sigma}{\sigma_0} = 1.03\left(\frac{V_{\rm esc}}{V}\right)^2 \quad (3.14)$$

or

$$\sigma = 1.03\pi(R_1 + R_2)^2(V_{\rm esc}/V)^2 . \quad (3.15)$$

TABLE 2

COALESCENCE CROSS SECTION

$V/V_{\rm esc}$	$R_{\rm fusion}/(R_1 + R_2)$	$\sigma/[\pi(R_1 + R_2)^2]$
$\to 0$	1.032	$1.032(V_{\rm esc}/V)^2$
0.46	0.59	3.14
0.84	0.355	0.629
1.12	0.236	0.244
1.67	0.128	0.062
2.33	0	0.0

The number of stellar coalescences that occur per unit time and volume is given by

$$\frac{dn}{dt} = \frac{1}{2} n_*^2 \gamma = \frac{1}{2} n_*^2 \langle \sigma V \rangle , \quad (3.16)$$

where n_* is the number of stars per unit and γ is the rate coefficient for coalescence. Each collision event involves two stars. In the rate coefficient, V is the pre-encounter relative velocity of each pair of colliding stars and σ is the coalescence cross section at that velocity, as given by Figure 11. The rate coefficient is averaged over all stars in the unit volume. If the stars have equal masses and follow a Maxwellian distribution of velocities, the rate coefficient is given by

$$\gamma = \langle \sigma V \rangle = \frac{4l^3}{\pi^{1/2}} \int_0^\infty V^3 \sigma e^{-l^2 V^2} dV \quad (3.17)$$

(Hills and Day 1976). Here

$$l^2 = \frac{3}{4\langle V^2 \rangle} , \quad (3.18)$$

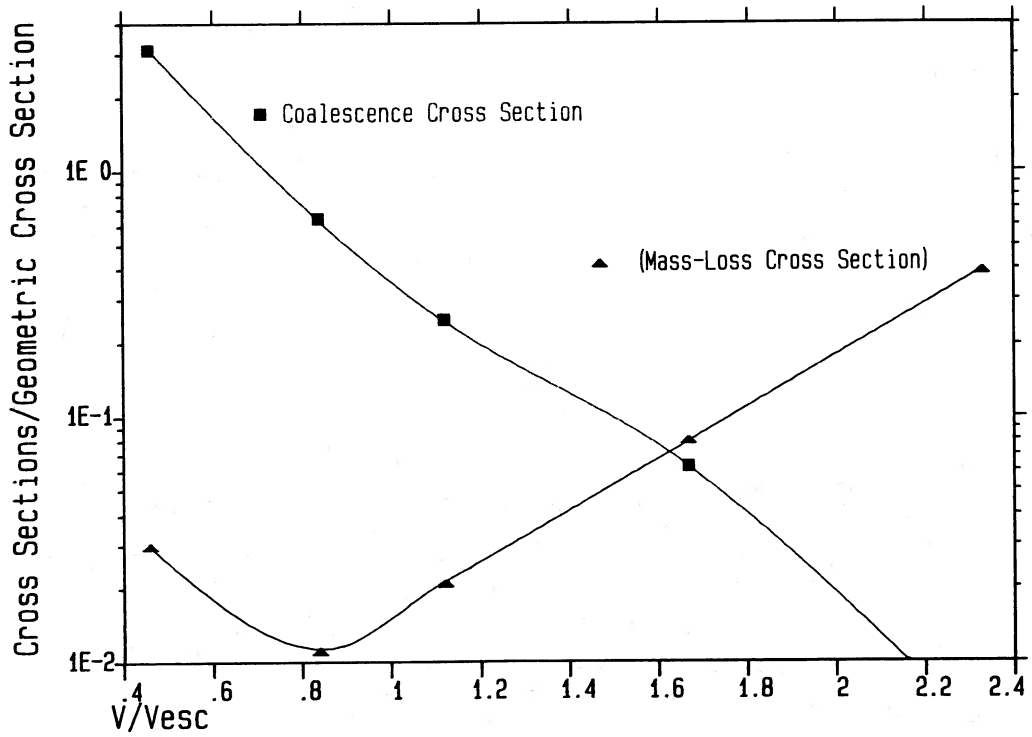

FIG. 11.—Cross sections for mass loss and coalescence as a function of the impact velocity. The impact velocity is given in units of the escape velocity from the surface of the two stars. The increase in cross sections at low impact velocity is due to gravitational focusing.

where $\langle V^2 \rangle$ is the mean squared velocity of the stars in the volume. We can use the values of σ given in Figure 11 in these equations to find the rate of stellar coalescence in systems having various velocity dispersions.

In the limit $V \to 0$, which is applicable to collisions in globular clusters where $V/V_{esc} \sim 10^{-2}$, we can integrate the equation for the rate coefficient analytically to give

$$\gamma = 1.03\pi(R_1 + R_2)^2 \left[\left(\frac{3}{\pi} \right)^{1/2} \left(\frac{V_{esc}^2}{\langle V^2 \rangle^{1/2}} \right) \right]. \quad (3.19)$$

ii) *Mass-Loss Cross Section*

The cross section for mass loss by collisions is given by

$$\sigma = \int_0^\infty A 2\pi p \, dp \, . \quad (3.20)$$

Here

$$2p \, dp = 2R_{min} \, dR_{min} + R_a \, dR_{min} \, , \quad (3.21)$$

so that

$$\sigma = \pi \int_0^\infty A(2R_{min} + R_a) dR_{min} \, , \quad (3.22)$$

$$= \pi \int_0^\infty A[2R_{min} + (R_1 + R_2)(V_{esc}/V)^2] dR_{min} \, . \quad (3.23)$$

Here $A = \Delta M/(M_1 + M_2)$, which is given in Figure 4, is the fractional mass loss when two stars collide with closest-approach distance R_{min}.

Table 3 gives the mass-loss cross section which was calculated for several values of (V/V_{esc}).

If $V \ll V_{esc}$, the equation for the mass-loss cross section reduces to

$$\sigma \to \pi \int_0^\infty A(R_1 + R_2)(V_{esc}/V)^2 dR_{min} \, . \quad (3.24)$$

TABLE 3

MASS-LOSS CROSS SECTIONS

V/V_{esc}	$\sigma/[\pi(R_1 + R_2)^2]$
$\to 0$	$0.0147(V_{esc}/V)^2$
0.46	0.0294
0.84	0.0112
1.12	0.0212
1.67	0.0792
2.33	0.391

Using our numerical values for A as a function of R_{min} for $V/V_{esc} = 0$ as given in Figure 4, we found that this limit

$$\frac{\sigma}{\pi(R_1 + R_2)^2} = 0.0147 \left(\frac{V_{esc}}{V} \right)^2 . \quad (3.25)$$

This result is applicable to collisions in globular clusters.

Figure 11 shows the cross sections for mass loss and coalescence plotted as a function of impact velocity. The coalescence cross section is much larger than the mass-loss cross section for most stellar systems, including globular clusters and galactic nuclei.

The amount of mass loss per unit time and volume resulting from stellar collisions is given by the equation

$$\frac{dM}{dt} = \frac{1}{2}(2M)n_*^2 \langle \sigma V \rangle = \frac{\rho_*^2 \langle \sigma V \rangle}{M} , \quad (3.26)$$

where σ is the cross section for mass loss given by Figure 11, $M = M_1 = M_2$ is the mass of the individual stars, and $\rho_* = Mn_*$ is the stellar mass density. If the stars follow a Maxwellian distribution of velocities, the mass-loss rate coefficient $\langle \sigma V \rangle$ can be found numerically by the same procedure used to determine the physical-coalescence rate coefficient, if the mass-loss cross section is substituted for the coalescence cross section.

IV. CONCLUSION

We have calculated physical collisions between stars treated as polytropes of index $n = 1.5$. The work is directly applicable to collisions between two lower–main-sequence stars, between two white dwarfs, and between two very massive upper–main-sequence stars whose internal structure is dominated by large convective cores. The results should be directly applicable to collisions between main-sequence stars in globular clusters and galactic nuclei and to the coalescence of massive stars bound gravitationally in a fragmentation hierarchical structure such as may be present in the embryonic subcluster R136a.

The extensive computations required for this project were done at Los Alamos National Laboratory. We would like to thank Mike Newman for invaluable help with computing over the two and a half years required to do this project. The work of W. B. at Los Alamos was supported by a Director's Postdoctoral Fellowship and by the Swiss National Science Foundation. His work at Harvard has been partially supported by the Swiss National Science Foundation and National Aeronautics and Space Administration grant NGR 22-007-272.

REFERENCES

Benz, W. 1984*a*, *Astr. Ap.*, **139**, 378.
Benz, W. 1984*b*, Ph.D. thesis, Geneva Observatory.
Benz, W., Slattery, W. L., and Cameron, A. G. W. 1986, *Icarus*, **66**, 515.
Colgate, S. 1967, *Ap. J.*, **150**, 163.
DeYoung, D. S. 1968, *Ap. J.*, **153**, 633.
Gingold, R. A., and Monaghan, J. J. 1977, *M.N.R.A.S.*, **181**, 373.
———. 1979, *M.N.R.A.S.*, **188**, 45.
———. 1981, *M.N.R.A.S.*, **197**, 461.
———. 1982, *J. Comput. Phys.*, **46**, 429.
———. 1983*a*, *M.N.R.A.S.*, **204**, 715.
———. 1983*b*, *J. Comput. Phys.*, **52**, 374.
———. 1985, *Astr. Ap.*, **149**, 1.
Hills, J. G. 1975, *Nature*, **254**, 295.
Hills, J. G. 1976, *Ap. Space Sci.*, **45**, 243.
———. 1978, *M.N.R.A.S.*, **182**, 517.
Hills, J. G., and Day, C. A. 1976, *Ap. Letters*, **17**, 87.
Lucy, L. B. 1977, *A.J.*, **83**, 1013.
Mathis, J. 1967, *Ap. J.*, **147**, 1050.
Ogorodnikov, K. F. 1965, *Dynamics of Stellar Systems* (New York: Pergamon), p. 314.
Ostriker, J. P., and Peebles, P. J. E. 1973, *Ap. J.*, **186**, 467.
Press, W. H., and Teukolsky, S. A. 1977, *Ap. J.*, **213**, 183.
Seidl, F. G. P., and Cameron, A. G. W. 1972, *Ap. Space Sci.*, **15**, 44 (SC).
Spitzer, L., and Saslaw, W. C. 1966, *Ap. J.*, **143**, 400.
Wood, D. 1981, *M.N.R.A.S.*, **194**, 201.

WILLY BENZ: Department of Astronomy, Harvard University, 60 Garden Street, Cambridge, MA 02138

JACK G. HILLS: Theoretical Astrophysics, T6, MS B288, Los Alamos National Laboratory, Los Alamos, NM 87545